Building a reduced model for nonlinear dynamics in Rayleigh-Bénard convection with counter-rotating disks

M. C. Navarro,[1,*] L. Martin Witkowski,[2,4] L. S. Tuckerman,[3] and P. Le Quéré[4]
[1]*Dpto. Matemáticas, Facultad de CC. Químicas, Univ. de Castilla La Mancha, Camilo José Cela s/n, 13071 Ciudad Real, Spain*
[2]*Université Pierre et Marie Curie-Paris 6, 4 place Jussieu, 75252 Paris, France*
[3]*PMMH-ESPCI, CNRS (UMR 7636), Univ. Paris 6 & 7, 10 rue Vauquelin, 75231 Paris, France*
[4]*LIMSI-CNRS (UPR 3251), BP 133, 91403 Orsay, France*
(Received 9 October 2009; published 26 March 2010)

A reduced model to decrease the number of degrees of freedom of the discretized Navier-Stokes equations to a small set that nevertheless captures the essential dynamics of the flow is proposed. The Rayleigh-Bénard convection problem in a cylinder of aspect ratio one where the lower and upper disks, maintained at hot and cold temperatures, respectively, rotate at equal and opposite angular velocities has been chosen to test the technique. The nonlinear dynamics is rich and complex when the temperature difference between disks and their angular velocity is varied. Representatives states—stationary, periodic near sinusoidal, and near heteroclinic—are presented. In each case, the reduced model is compared with temporal integration, and we show that 41 degrees of freedom are sufficient to reproduce the signal. We discuss the strengths and weaknesses of the algorithm by which we build our reduced model.

DOI: 10.1103/PhysRevE.81.036323 PACS number(s): 47.20.Ky, 47.20.Bp, 47.10.Fg, 02.70.Hm

I. INTRODUCTION

The development of techniques to reduce the number of degrees of freedom of nonlinear complex problem is an active research area. In fluid mechanics, the use of proper orthogonal decomposition (POD) has emerged and seems to be favored mainly for open flow problems [1–6] and, to a lesser extent, in confined geometries [7,8]. A POD basis is orthogonal and is optimal in the sense of minimizing the number of basis functions necessary to capture the energy of the flow. It nevertheless has the drawback of requiring results from a time-dependent code in order to acquire the "snapshots" to build the basis and this basis will inherently contain the germs of the initial condition used to run the simulation [9]. This can be a major problem in the context of bifurcation theory as it will favor certain solution branches, in particular the stable ones.

An alternate set of basis functions, which does not have such a bias, is formed by the leading eigenvectors (i.e., those corresponding to the eigenvalues with the largest real part) obtained from the governing equations linearized about a base state. As in the case of POD, the set of basis functions must be tailored to each specific problem. Even though there is no mathematical justification for this choice, as rapid convergence of the expansion is not ensured, the reduced set of leading eigenvectors seems to be a very good candidate for a Galerkin projection basis and captures most of the dynamics of the flow. Reduced models and control strategies based on leading eigenvectors have been implemented for open cavity flows [10] and compared with results of POD models [11]. Reduced models can also be constructed from the eigenfunctions of the Stokes problem, as was done for the flow around an array of cylinders [12].

Several previous studies have used an eigenvector basis to study convective problems in small-aspect ratio cylindrical domains. Dauby *et al.* [13] studied the three-dimensional Marangoni-Bénard instability, while Siggers [14] studied axisymmetric Rayleigh–Bénard convection. In both problems, the base flow, a purely conductive state, is available analytically. Siggers [14] used stress-free boundary conditions, for which the eigenpairs can also be calculated analytically, while Dauby *et al.* [13] computed the eigenpairs numerically for realistic rigid boundaries. Both studies were able to construct bifurcation diagrams and to capture heteroclinic cycles. Gadoin *et al.* [15] studied a differentially heated cavity that has a nontrivial base flow. They were able to reproduce accurately the transient signal of a decaying random small amplitude two-dimensional perturbation.

We extend these studies by choosing a problem which combines two well-known fluid-mechanical configurations: Rayleigh-Bénard convection in cylindrical geometry, e.g., [16] and the flow generated by two exactly counter-rotating disks, e.g., [17]. For a given aspect ratio and fluid properties, this combination leads to a problem described by two parameters, namely the temperature difference between the upper and lower bounding disks, measured by the Rayleigh number Ra, and their angular velocity, measured by the Reynolds number Re. We restricted our reduced model to the axisymmetric case in order to compare its results with those of a fully resolved calculation, which uses the Newton-Arnoldi method to compute the bifurcation diagram in the two-parameter (Re, Ra) space. A companion article [18] presents the results of this analysis, which includes interesting dynamics such as relaxation oscillations and bistability. Our purpose here is to show that a reduced model using a modest number of eigenvectors of a numerically computed base flow can reproduce phenomena such as these, far beyond the threshold.

The paper is organized as follows. Section II presents the physical setup, and the general mathematical formulation of

*Corresponding author. FAX: +34 926295318; mariacruz.navarro@uclm.es

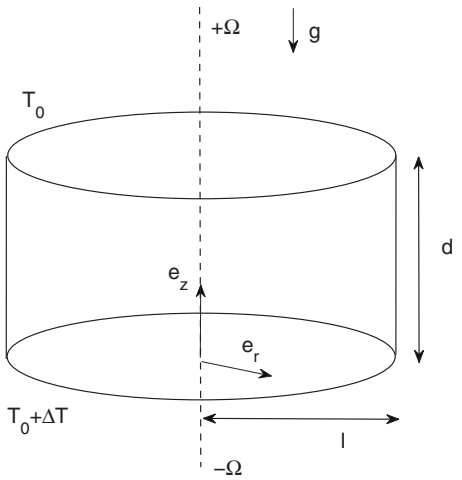

FIG. 1. Physical setup.

the problem in a dimensionless form. Section III describes our reduced model and Sec. IV describes its numerical implementation using a spectral method. In Sec. V, numerical results obtained using the reduced model are presented and compared to those obtained from fully resolved simulations. Section VI describes our attempts to minimize the number of degrees of freedom required to obtain reasonable agreement with fully resolved simulations. In Sec. VII, we discuss the prospects for extending our model to treat three-dimensional geometries and to perform bifurcation analysis.

II. FORMULATION OF THE PROBLEM

The physical setup (see Fig. 1) consists of a horizontal fluid layer in a cylindrical container with aspect ratio $\Gamma = l/d = 1$. The walls are rigid and the temperature at the upper and the bottom plates are T_0 and $T_0+\Delta T$, respectively. We assume axisymmetry throughout.

In the governing equations, $\mathbf{u}=(u_r,u_\phi,u_z)$ is the velocity field, T is the temperature, p is the pressure, r is the radial coordinate, and t is the time. They are expressed in dimensionless form after rescaling: $\mathbf{r}'=\mathbf{r}/d$, $t'=\kappa t/d^2$, $\mathbf{u}'=d\mathbf{u}/\kappa$, $p'=d^2p/(\rho_0\kappa\nu)$, and $\Theta=(T-T_0)/\Delta T-0.5$. Here $\mathbf{r}$ is the position vector, κ the thermal diffusivity, ν the kinematic viscosity of the liquid, and ρ_0 the mean density at temperature T_0. The domain is $\mathcal{D}=[0,\Gamma]\times[-1/2,1/2]$.

The system evolves according to the momentum, mass balance and energy conservation equations, which in dimensionless form (with primes now omitted) are,

$$\nabla\cdot\mathbf{u}=0, \tag{1}$$

$$\partial_t\Theta+\mathbf{u}\cdot\nabla\Theta=\nabla^2\Theta, \tag{2}$$

$$\partial_t\mathbf{u}+(\mathbf{u}\cdot\nabla)\mathbf{u}=\mathrm{Pr}(-\nabla p+\nabla^2\mathbf{u}+\mathrm{Ra}\Theta\mathbf{e}_z), \tag{3}$$

where the operators and fields are expressed in cylindrical coordinates and the Oberbeck-Bousinesq approximation has been used. Here $\mathbf{e}_z$ is the unit vector in the z direction. The following dimensionless numbers have been introduced: the Prandtl number $\mathrm{Pr}=\nu/\kappa$, which is set to 1 in our study, and the Rayleigh number $\mathrm{Ra}=g\alpha\Delta Td^3/\kappa\nu$, which represents the effect of buoyancy and in which α is the thermal-expansion coefficient and g the gravitational acceleration.

Regarding boundary conditions, the top and bottom disks turn at the same angular velocity Ω but in opposite directions and the lateral wall is rigid, so

$$u_r=u_z=0, \quad u_\phi=\pm\,\mathrm{Pr}\,\mathrm{Re}\cdot r \quad \text{at} \quad z=\pm\,1/2, \tag{4}$$

$$u_r=u_z=u_\phi=0 \quad \text{at} \quad r=\Gamma \tag{5}$$

where $\mathrm{Re}=\Omega d^2/\nu$ is the Reynolds number. For the temperature we consider isothermal top and bottom disks and a lateral insulating wall,

$$\Theta=\mp\,0.5, \quad \text{at} \quad z=\pm\,1/2 \quad \text{and} \quad \partial_r\Theta=0 \quad \text{at} \quad r=\Gamma. \tag{6}$$

Regularity conditions [19] are imposed at $r=0$. The discontinuity in u_ϕ at $r=\Gamma$, $z=\pm\,1/2$ has been regularized by connecting smoothly the linear profile $u_\phi=\pm\,\mathrm{Pr}\,\mathrm{Re}\cdot r$ at $z=\pm\,1/2$ with the condition $u_\phi=0$ at $r=\Gamma$ by means of a local exponential profile,

$$u_\phi(r,\pm\,1/2)=\begin{cases}\pm\,\mathrm{Pr}\,\mathrm{Re}\cdot r & \text{if } r\in[0,r_0]\\ \pm\,\mathrm{Pr}\,\mathrm{Re}\cdot r\pm\dfrac{\mathrm{Pr}\,\mathrm{Re}\cdot r}{1-e^{-(\Gamma-r_0)^2}}(-1+e^{-(r-r_0)^2}) & \\ \qquad\qquad \text{if } r\in[r_0,\Gamma]\end{cases}$$

where r_0 is a value of r close to Γ.

III. REDUCED MODEL

In this section we present a method to reduce Eqs. (1)–(6) to a low-order differential system capable of representing the dynamics of the flow. This reduction follows the approaches presented in, e.g., [15,20].

The solution $U(r,z,t)=(\mathbf{u},\Theta,p)(r,z,t)$ of Eqs. (1)–(3) at given Re and Ra is expressed as

$$U(r,z,t)=U^b(r,z)+\tilde{U}(r,z,t) \tag{7}$$

where $U^b(r,z)$ is the base flow for the given Re and Ra numbers and $\tilde{U}(r,z,t)$ the perturbation. Introducing Eq. (7) into the full system [Eqs. (1)–(3)], the time evolution equation for $\tilde{U}(r,z,t)$ can be written as

$$\partial_t\tilde{U}=\mathcal{L}_{U^b}\tilde{U}-\mathcal{N}\tilde{U} \tag{8}$$

where $\mathcal{L}_{U^b}$ describes the linear part of the equations governing the perturbation; see Eqs. (A2) and (A3) in the Appendix. The nonlinear quadratic part $\mathcal{N}$ can be represented, somewhat schematically, as $\tilde{U}\cdot\nabla\tilde{U}$; again, see the Appendix. Our basis functions are the eigenvectors $\xi_k(r,z)$ of $\mathcal{L}_{U^b}$, satisfying $\mathcal{L}_{U^b}\xi_k(r,z)=\lambda_k\xi_k(r,z)$. We decompose $\tilde{U}(r,z,t)$ into the form

$$\tilde{U}(r,z,t)=\sum_k A_k(t)\xi_k(r,z) \tag{9}$$

where the $A_k(t)$'s are the expansion coefficients corresponding to the eigenvectors $\xi_k(r,z)$. Inserting this expansion into Eq. (8) yields

$$\sum_k \frac{dA_k(t)}{dt}\xi_k(r,z) = \sum_k \lambda_k A_k(t)\xi_k(r,z) - \sum_{l,m} A_l(t)A_m(t)\xi_l(r,z)\cdot\nabla\xi_m(r,z). \tag{10}$$

On the right-hand side, the first sum corresponds to the linear part and the double sum to the nonlinear quadratic part. In order to obtain the low-order differential system we take the inner product of Eq. (10) with the eigenvectors $\eta_k(r,z)$ of the adjoint of the Jacobian, using the inner product $\langle f,g\rangle = 2\pi\int\int_{\mathcal{D}} f^* g r dr dz$, where f^* is the complex conjugate of f. The set of eigenvectors ξ_i is biorthogonal to η_i, i.e., $\langle \xi_i(r,z), \eta_k(r,z)\rangle = \delta_{ik}$. Using this property, the following nonlinear differential system of equations can be derived,

$$\frac{dA_k}{dt} = \lambda_k A_k - \sum_{l,m} \mu_{klm} A_l A_m \tag{11}$$

where $\mu_{klm} = \langle \xi_l(r,z)\cdot\nabla\xi_m(r,z), \eta_k(r,z)\rangle$. If the series in Eq. (9) is truncated with K terms, the number of degrees of freedom of the original equations is then reduced to K.

From now on, we will refer to this reduced model as RM. The reduced model takes the following algorithmic form.

Algorithm

1. Preprocessing

(i) Step 1. For a given Re and Ra compute the steady base state [time-independent solution of Eqs. (1)–(6)] using a Newton iterative method.

(ii) Step 2. Compute the K leading eigenvalues and eigenvectors (λ_i, η_i) and (λ_i, ξ_i) for $i=1,\ldots K$, from the direct and adjoint system, respectively, ordered by decreasing real part.

(iii) Step 3. Compute the inner products $\mu_{klm} = \langle \xi_l(r,z)\cdot\nabla\xi_m(r,z), \eta_k(r,z)\rangle$ for $k,l,m=1,\ldots,K$.

2. Time integration

(iv) Step 4. Starting with an initial condition $A_k(0)$, $k=1,\ldots,K$, integrate in time the system $\frac{dA_k}{dt} = \lambda_k A_k - \Sigma_{l,m}\mu_{klm}A_l A_m$, $k=1,\ldots,K$ gives $A_k(t)$, $k=1,\ldots,K$.

3. Postprocessing

(v) Step 5. Construct the state $U(r,z,t) = U^b(r,z) + \Sigma_k A_k(t)\xi_k(r,z)$.

IV. NUMERICAL IMPLEMENTATION

The reduced model and algorithm presented above can be used with any discretization (spectral basis, finite elements, and finite differences) of the original equations (base flow, linear stability system, and adjoint system). Gadoin *et al.* [15] chose finite differences. In the present work, we use a spectral method by expanding the fields in Chebyshev polynomials

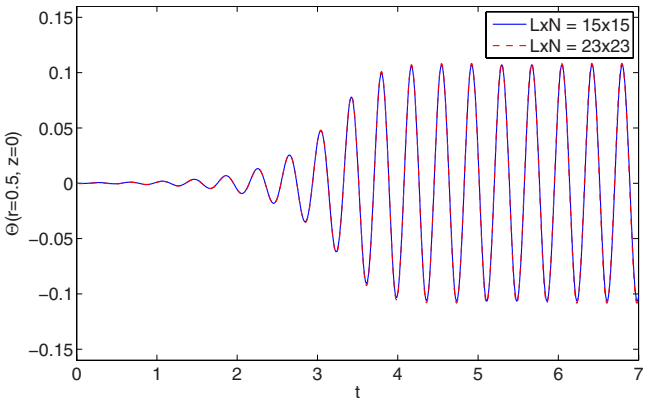

FIG. 2. (Color online) Comparison of spatial resolutions in an oscillating regime. Time series for $\Theta(0.5,0)$ for case *P*Ia (Re $=110$, Ra$=18\,000$). Solid blue curve: spatial grid $L=N=15$. Dashed red curve: spatial grid $L=N=23$. Both time series are computed using RM with $K=15$ eigenvectors. The two time series are so close as to be indistinguishable on the scale of the figure.

$$f(r,z) = \sum_{l=0}^{L-1}\sum_{n=0}^{N-1} f_{ln} T_l(r) T_n(z) \tag{12}$$

and evaluating at the Gauss-Lobatto collocation points (see Refs. [21,22]). For our computations, we use $L=N=15$. Figure 2 shows that the time series from a limit cycle (case *P*Ia, see Sec. V below) computed from our reduced model using our spatial resolution $L=N=15$ is close enough to that obtained using the finer resolution $L=N=23$ to be visually indistinguishable in Fig. 2. We have compared eigenvalues corresponding to the $L=N=15$ and the $L=N=23$ grids for three cases at Ra$=18000$ that we will study below; the differences are on the order of 0.001% for Re$=60$ (case *S*II), 0.01% for Re$=70.73$ (case *P*IIa), and 0.1% for Re$=110$ (case *P*Ia). For Reynolds numbers beyond this range, Ekman boundary layers appear near the rotating disks. These become increasingly thin with increasing Re, and accurate computation of eigenvalues and eigenfunctions would require higher resolution, as detailed in Lopez *et al.* [23]. For the range that we have studied, the spatial resolution $L=N=15$ is sufficient.

The discrete version of the eigenvalue problem for the direct and adjoint systems (see the Appendix) are solved (after a Cayley transformation [24]) with eigs, the MATLAB implementation of ARPACK [25]. We calculated 50 eigenpairs using a Krylov space of dimension 160, obtaining residual errors that were between 10^{-8} and 10^{-11}. More details on steps 1 and 2 of the algorithm can be found in Ref. [26].

In order to compute the inner products μ_{klm} in step 3, we interpolate the velocity and temperature fields onto a uniform 300×300 grid and use Simpson's rule. In step 4, any integration standard routine can be used. We chose ode45 in MATLAB.

Because we have sought to measure only the error due to truncating the eigenvector basis set, all other steps—in particular, the residual in Newton's method for the steady base state, calculation of the eigenpairs, and time integration of the reduced model—have been carried out to machine precision or very high accuracy and can be viewed for the pur-

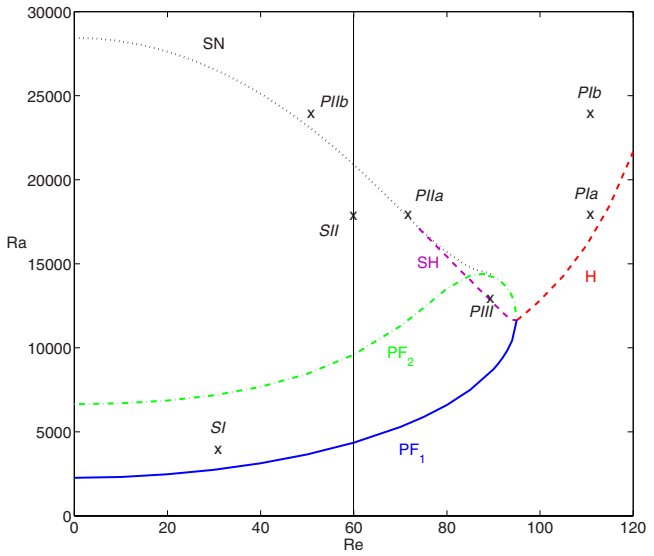

FIG. 3. (Color online) Curves of bifurcation points in the (Re, Ra) plane showing first pitchfork bifurcation (blue, solid, PF_1), second pitchfork bifurcation (green, dash-dotted, PF_2), Hopf bifurcation (red, dashed, H), secondary subcritical Hopf bifurcation (violet, dashed, SH) and saddle-node bifurcation (black, dotted, SN). The vertical line at Re=60 relates to the bifurcation diagram represented in Fig. 3. Crosses indicate steady (SI, SII) and periodic (PIa,b, $PIIa,b$, $PIII$) cases selected for detailed study.

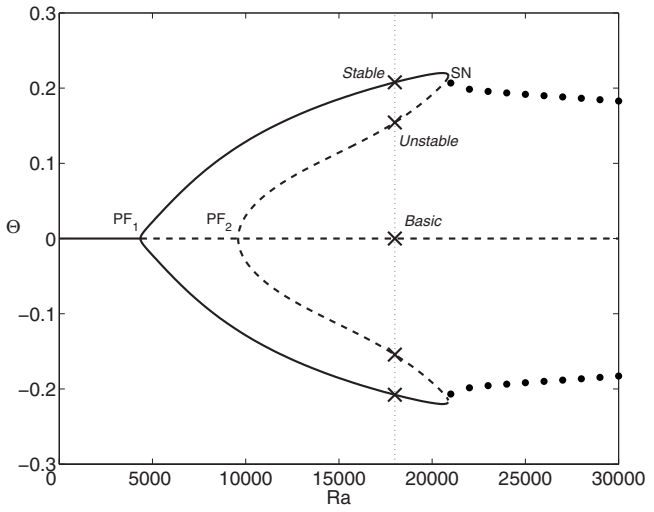

FIG. 4. Bifurcation diagram corresponding to the vertical line in Fig. 3. Temperature Θ at (r=0.5, z=0) as a function of Ra at Re =60. At Ra=18 000, five steady states (crosses) are found. For Ra >20 900, dots represent the limit cycle. The lower part of the diagram is related to the upper part by the Boussinesq reflection symmetry of Eq. (13). Upper two states represented by crosses are shown in Figs. 9 and 10.

poses of this investigation as exact; the error is largely dominated by that due to the basis set truncation.

The full time-integration code used for comparison is completely independent of the reduced model. The code is implemented with a stream-function-vorticity formulation as described in [27,28] in an isothermal context, with slight modifications in boundary-condition implementation [29]. The resolution used is a uniformly distributed (51×51) mesh. A typical time step is 10^{-4}. We will refer to the fully resolved time-integration code as FT.

V. NUMERICAL RESULTS

In this section we demonstrate the ability of the RM to reproduce different temporal behaviors appearing for different values of parameters Re and Ra. Figure 3 is a phase diagram in the (Re, Ra) plane, showing the bifurcations that occur in FT; see [18]. There are two pitchfork bifurcations, indicated in Fig. 3 as PF_1 and PF_2, a saddle-node bifurcation indicated as SN, a Hopf bifurcation indicated as H, and a secondary subcritical Hopf bifurcation indicated as SH. These curves delimit various regions in the (Re, Ra) plane, in which system behaves differently. Below PF_1 and H, the only solution is a steady state which is symmetric, meaning that it is invariant under reflection in the equatorial (z) plane, combined with temperature inversion

$$(u_r,u_\theta,u_z,\Theta)(r,z)\rightarrow(u_r,u_\theta,-u_z,-\Theta)(r,-z). \qquad (13)$$

This basic state, belongs to the branch that originates at (Re, Ra)=(0,0). For Re<95 and Ra above PF_1, this state is unstable and there also exist two asymmetric stable steady states. Above PF_2, there exist two additional asymmetric unstable states, leading to a total of five steady states, as illustrated in the bifurcation diagram in Fig. 4 for Re=60. (The

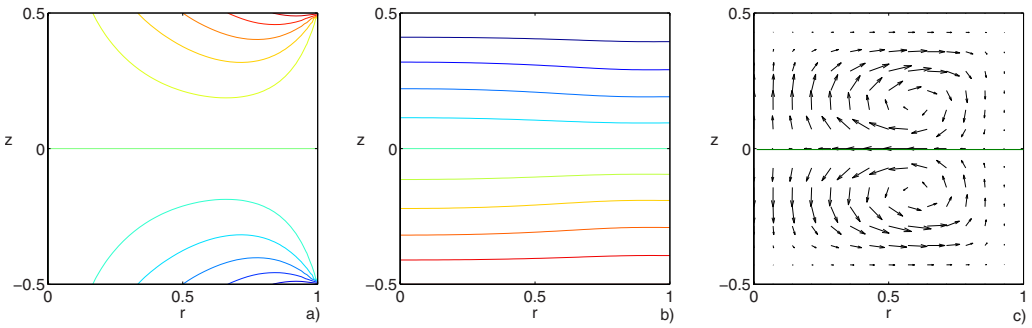

FIG. 5. (Color online) Basic state, which is symmetric and unstable, for SI (Re=30, Ra=4000). (a) u_ϕ (b) temperature Θ (c) meridional velocity (u_r,u_z) and the streamline separating the rolls (solid green curve). Here and in subsequent figures, the contours correspond to equally spaced values within their ranges of [−Re:Re] for u_ϕ and [−0.5:0.5] for Θ.

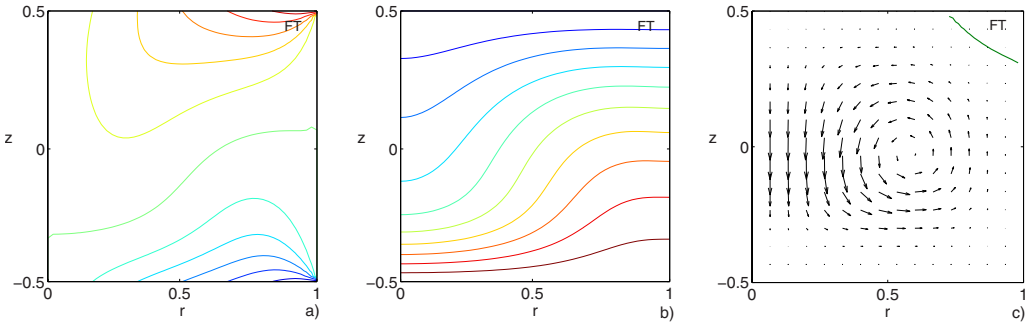

FIG. 6. (Color online) Stable state for Re=30, Ra=4000. (a) u_ϕ (b) temperature Θ (c) meridional velocity (u_r, u_z) and the streamline separating the rolls (solid green curve).

basic state can be stable or unstable, depending on the values of Re and Ra. When not otherwise specified, "stable state" will refer to the stable asymmetric state produced at bifurcation PF_1 and "unstable state" will refer to the unstable asymmetric state produced at bifurcation PF_2. For Re$>$95, above H, the asymptotic behavior is a limit cycle. Near the SN and SH curves, there is a transition between steady and oscillatory behavior. The analysis of this transition is quite complicated and is described in detail in the companion article [18].

We set seven representative points (see Fig. 3) at which the method is tested: the two first cases, *S*I (Re=30, Ra=4000) and *S*II (Re=60, Ra=18 000), correspond to steady flow above the convective threshold. In *S*I we are close to the threshold and far from it in case *S*II (beyond the second pitchfork bifurcation). The rest of the cases considered correspond to temporally periodic flows. For *P*Ia (Re=110, Ra=18 000), close to the Hopf bifurcation curve, and *P*Ib (Re=110, Ra=24 000), far from it, time series will present nearly sinusoidal behavior. For the second periodic case, *P*IIa (Re=70.73, Ra=18 000) and *P*IIb (Re=50, Ra=24 000), we are close to the saddle-node bifurcation (which takes place at Re=70.7 for Ra=18 000 and Re=46.2 for Ra=24 000) and the oscillations are near heteroclinic. Finally, *P*III (Re=88.5, Ra=13 000) presents an example of the ability of RM to deal with the dynamics near the secondary subcritical Hopf bifurcation. We recall that multiple steady states can exist; for example, for *S*II, Fig. 4 shows five different steady states, while for *P*III there is coexistence of a limit cycle with steady states. In every case, $K \leq 41$, meaning that no more than 41 leading eigenvalues (those with the largest real part) and their associated eigenvectors are used. Results will be presented starting from the simplest cases.

A. Stationary case I: close to the threshold

We start by analyzing the case *S*I (Re=30, Ra=4000). In the absence of rotation, i.e., Re=0, the solution for subcritical values of Ra is the well-known conductive state in which there is no motion and the temperature varies linearly in z.

For a nonzero value of Re the basic solution defined above is qualitatively similar to the conductive solution, but no longer has a simple analytic form and must be computed with Newton's method. An example can be found in Fig. 5, where the azimuthal velocity, isotherms, and meridional velocity field of the basic state at Re=30, Ra=4000 are shown. The temperature field is close to the linear conductive profile. Two weak large symmetric recirculating cells are found for the meridional velocity field. The azimuthal velocity increases gradually from negative in the lower part of the cylinder to positive in the upper part, following the counter-rotating disks.

In region *S*I, the basic state has one unstable eigenmode, so time integration starting from basic leads to the convective stable state shown in Fig. 6. Isotherms, velocity field and azimuthal velocity are presented. Symmetry with respect to the $z=0$ plane is broken. The velocity field contains two rolls, a larger one in the center of the cell and a smaller one in the upper right corner, which has been made visible by drawing the streamline separating the rolls. Isotherms and azimuthal velocity are convected by the meridional motion.

It is a first verification for RM to reach the stable state (Fig. 6) when a perturbation is applied to the basic state (Fig. 5). After transition, the expansion coefficients $\{A_k\}_{k=1}^K$, solution of system (11), are constant in time. Isotherms of the constructed stable state $U(r,z)=U^b(r,z)+\Sigma_{k=1}^K A_k \xi_k(r,z)$ are shown in Fig. 7(a) for $K=15$ in comparison to those obtained with the fully resolved temporal code FT. There is a good agreement between both solutions, as for the rest of the fields.

In order to quantify the error, we define

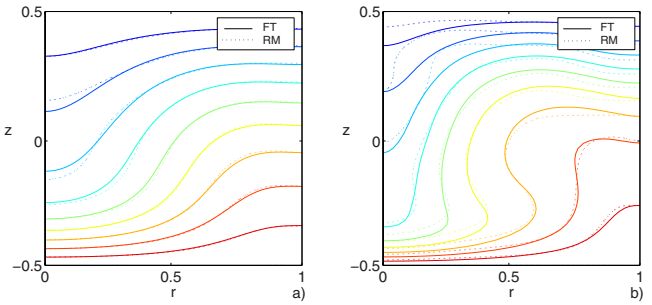

FIG. 7. (Color online) Isotherm comparison for stable state computed using FT (solid curves) and RM (dashed curves). (a) Case *S*I (Re=30, Ra=4000) with $K=15$; (b) case *S*II (Re=60, Ra=18 000) with $K=41$.

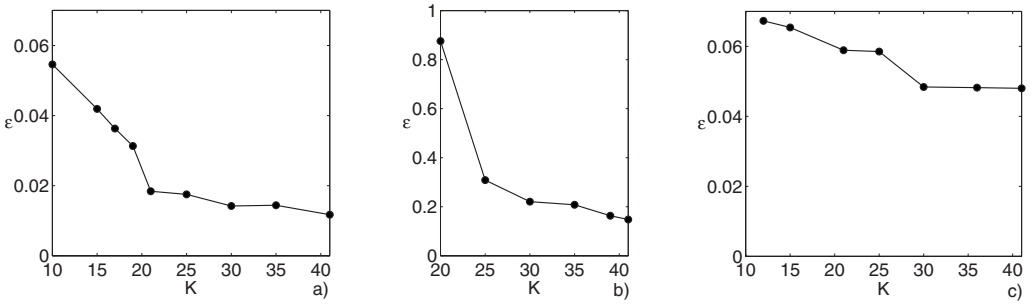

FIG. 8. Error $\epsilon = \|U_{FT} - U_{RM}\| / \|U_{FT}\|$ as a function of K for (a) SI (Re=30, Ra=4000); (b) SII (Re=60, Ra=18 000); and (c) PIa (Re=110, Ra=18 000) at time $t=t_1$.

$$\epsilon \equiv \|U_{FT} - U_{RM}\| / \|U_{FT}\|,$$

where U_{FT} is computed with FT and U_{RM} with RM, and $\| \, \|$ is the L_2 norm over the domain $\mathcal{D}$. A plot of ϵ as a function of K is presented in Fig. 8(a) for the case SI (Re=30, Ra=4000). We find that ϵ is of order $O(10^{-2})$ and decreases as K increases.

B. Stationary case II: far from the threshold

The second region analyzed goes beyond the second pitchfork bifurcation and includes an area far from the threshold. We choose the parameter values (Re=60, Ra=18 000) to represent this region.

In this region, the basic state resembles that in SI (see Fig. 5) but has two real positive eigenvalues. There exist two asymmetric unstable states (also computed with Newton's method) one of which is shown in Fig. 9. Starting from either of these states as initial conditions, time integration leads to the stable state in Fig. 10, which resembles that described in region SI.

Figure 7(b) compares the solutions of RM for $K=41$ (dashed line) and of FT (solid line). The error ϵ quantifying the difference between U_{FT} and U_{RM} is shown in Fig. 8(b). The error is large [almost order $O(1)$] for smaller values of K and a large value of K is needed to obtain acceptable $[O(10^{-1})]$ values of ϵ. (We note that we have experimented with another set of eigenvectors, obtained by linearizing around the unstable state, and have obtained satisfactory agreement using K as small as 25. But since there is no systematic means of choosing a state other than the basic state about which to linearize, we do not present these results here.)

C. Periodic orbit I: near-sinusoidal limit cycle

We now describe the tests of the temporally periodic orbits. We start with the limit cycle that appears in the (Re, Ra) plane above the Hopf bifurcation but far from the SN curve as in PIa (Re=110, Ra=18 000) and PIb (Re=110, Ra=24 000). In this region, the basic state has a pair of complex-conjugate eigenvalues with positive real parts. Figure 11 (solid curve) shows the time series for temperature at $r=0.5$, $z=0$ in the case PIa. This is the quantity which will be plotted for all periodic orbits. A near-sinusoidal periodic behavior is clearly observed. In Fig. 12, the fields are shown at two instants during the cycle, $t=t_1$ and $t=t_2$ (those indicated in Fig. 11). The limit cycle has spatiotemporal symmetry: the states in the second half of the cycle are related by reflection symmetry to those in the first half of the cycle. The vortex in the upper right corner is smaller during the first half of the cycle [see Fig. 12(c)] and larger during the second half [see Fig. 12(f)]. The expansion coefficients $\{A_k(t)\}_{k=1}^{K}$ computed with RM to construct the flow are periodic in time. The time series for the temperature obtained by using RM with $K=15$ is plotted in Fig. 11 (dashed curve) where it is compared with the solution computed via FT (solid curve). Good agreement is achieved in both amplitude and period of the orbit, with relative errors of 3.7% and 4.1%, respectively.

In addition to comparing the time series of $\Theta(0.5,0)$, we have also compared the entire fields U_{FT} and U_{RM} at time $t=t_1$ (upper row of Fig. 11). Figure 8(c) shows the error ϵ as

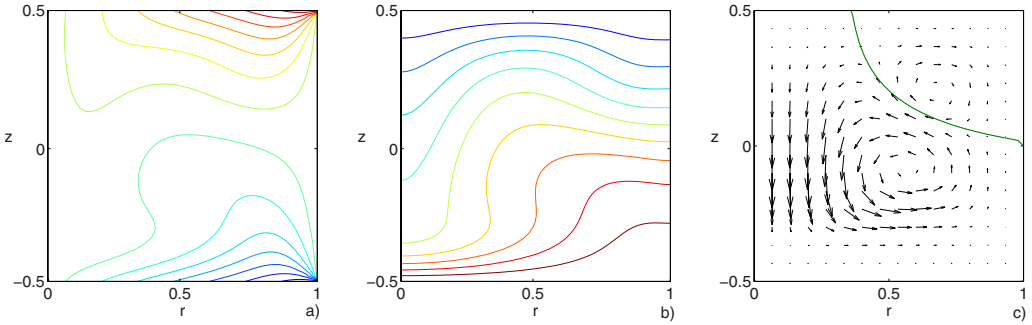

FIG. 9. (Color online) Unstable state in region SII (Re=60, Ra=18 000). (a) u_ϕ (b) temperature Θ (c) meridional velocity (u_r, u_z) and the streamline separating the rolls (solid green curve).

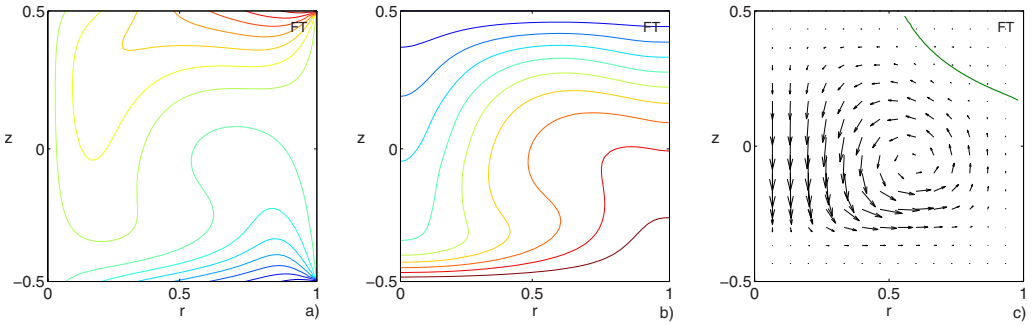

FIG. 10. (Color online) Stable state in region *S*II (Re=60, Ra=18 000). (a) u_ϕ (b) temperature Θ (c) meridional velocity (u_r, u_z) and the streamline separating the rolls (solid green curve).

a function of K. It is found to be of order $O(10^{-2})$ and becomes smaller as K increases, as in the stationary case. The same behavior is observed for *P*Ib, the only difference being that the minimum K used to achieve good results is larger ($K=27$) as will be discussed in Sec. VI.

D. Periodic orbit II: near-heteroclinic cycle

We now discuss cases *P*II, just beyond the saddle-node curve SN. Starting at a *P*I case and decreasing Re, the periodic cycles become less smooth as Re, with near-heteroclinic cycles are found close to the saddle-node bifurcation. The oscillations consist mainly of two long plateaus with abrupt gradients between them. Figure 13 (solid curve) shows this for *P*IIa (Re=70.73, Ra=18 000). Figure 14 shows the solution fields at times $t=t_1$ and $t=t_2$, marked in Fig. 13. The limit cycles, during which the smaller vortex is alternately in the upper [Fig. 14(c)] and lower [Fig. 14(f)] right corners, become increasingly complex as the saddle-node bifurcation is approached, as reported in Ref. [18]. The period increases dramatically until, precisely at the saddle node, the period becomes infinite and the cycle is heteroclinic. RM has been tested near this heteroclinic cycle. Figure 13 shows the agreement between solutions obtained with FT and with RM for $K=37$. Results from RM (dashed curve) are in reasonable agreement with FT and the relative errors in period and amplitude are 13% and 1.8%, respectively. The large error in the period is not surprising, given that the period varies sharply with Re in this parameter region: RM gives 4.95, while FT gives 4.34 for Re=70.73 and 5.48 for Re=70.71.

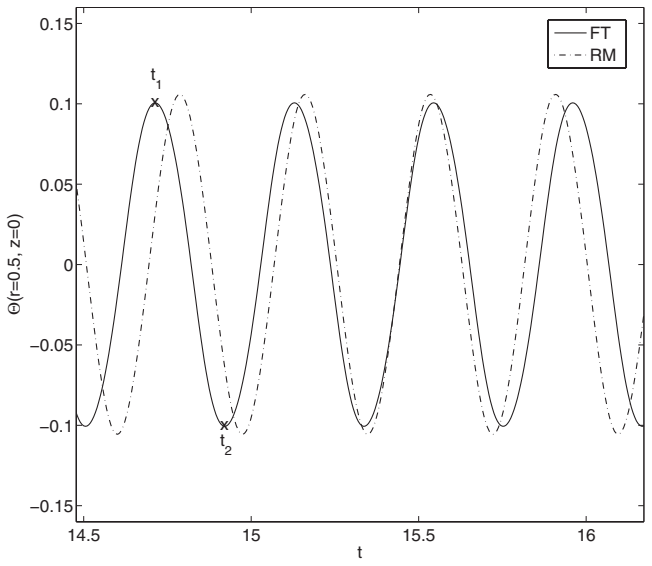

FIG. 11. Time series for $\Theta(0.5,0)$ obtained with FT (solid curve) and RM for $K=15$ (dashed curve). Case *P*Ia (Re=110, Ra =18 000). Instantaneous flows at times t_1 and t_2 are shown in Fig. 12.

E. Periodic orbit III: secondary subcritical Hopf bifurcation

The reduced model RM has also been able to reproduce the temporal behavior near the secondary subcritical Hopf bifurcation. Figure 15 (solid curve) shows the time series for the temperature obtained with FT for two different initial conditions at *P*III (Re=88.5, Ra=13 000). As shown in Ref. [18], there are multiple stable solutions in this range: either a periodic orbit or the stable steady state can be obtained. The periodic signal is attained for FT by setting the angular velocity of the upper disk to zero for $t=0$ to $t=2$, and for RM by setting all A_k initially to 0.01. RM with $K=27$ generates the same signal (dashed curve) as that obtained with FT (solid curve) and the agreement between the solutions is good, with relative errors of values 14% and 2.3% for the period and amplitude respectively. The stable steady solution is obtained for FT by gradually increasing Re at a given Ra, while for RM, it is obtained by setting all A_k initially to (-10^{-4}). The relative error is 5.4%.

VI. OPTIMIZING THE REDUCED MODEL

Decreasing K greatly reduces the computation time, since the computation time per time step is proportional to K^3. In this section, we describe numerical experiments we have carried out to reduce K.

The choice of a minimal model has been a central point of much previous research, and has led to various hybrid approaches. Guided by physical and dynamical-systems considerations, Noack *et al.* [1,4] added modes to their POD models corresponding to the temporal mean flow and to the pressure. Bangia *et al.* [12] modeled some damped modes by slaving, i.e. assuming their amplitudes adjust instantaneously to those of the active modes. One of the models studied by

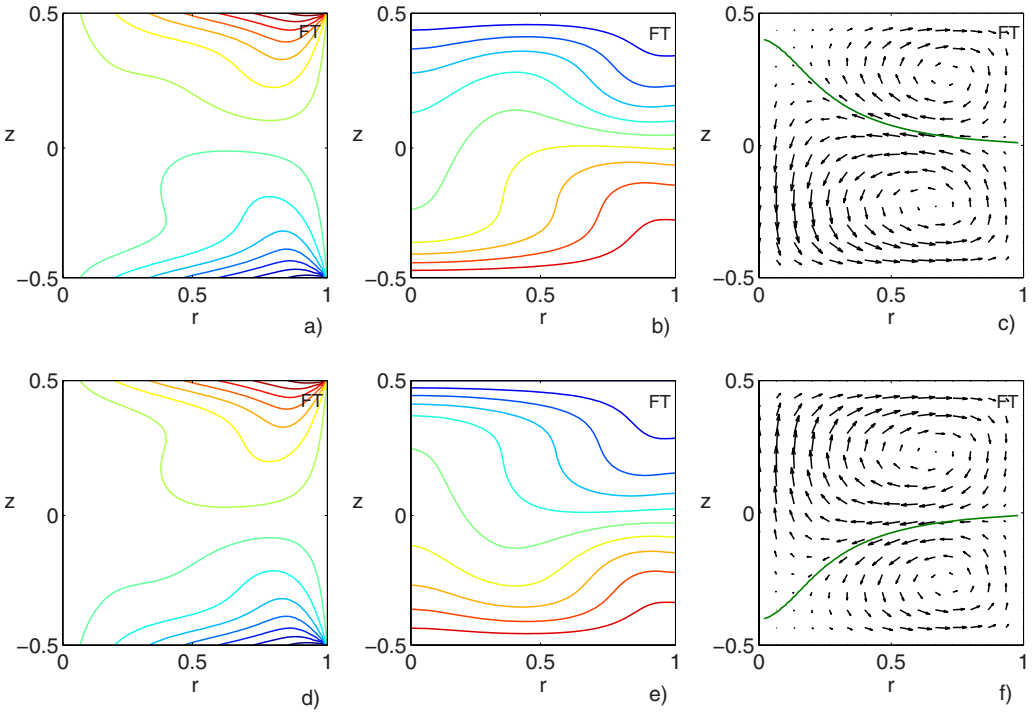

FIG. 12. (Color online) Instantaneous flows for *P*Ia (Re=110, Ra=18 000). Upper row: flow at instant $t=t_1$ of Fig. 11. (a) u_ϕ (b) Θ (c) meridional velocity (u_r,u_z). Lower row: flow at $t=t_2$ (d) u_ϕ (e) Θ (f) meridional velocity (u_r,u_z). In Figs. 12(c) and 12(f) the solid green curve represents the streamline separating the rolls. The two instantaneous flows are related via reflection symmetry (13).

Barbagallo *et al.* [11] combines unstable (growing) eigenvectors with stable (damped) POD modes.

Our criterion for choosing eigenmodes in step 2 is the real part of the corresponding eigenvalue; this is straightforward but may incorporate unnecessary modes. We have attempted to additionally sort eigenmodes based on the magnitude of the inner products μ_{klm} computed in step 3 which determine the nonlinear interaction between the modes, but we found no conclusive criterion for this *a priori* search. We then proceed to sort the modes by their amplitudes $|A_k|$. Since this *a posteriori* sorting necessarily occurs after the computation, it

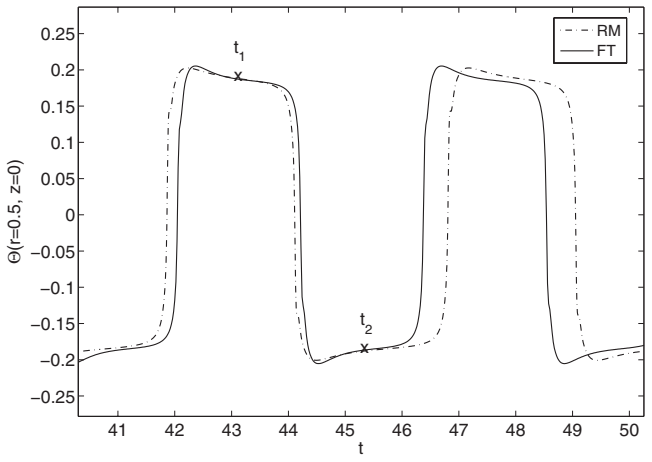

FIG. 13. Time series for $\Theta(0.5,0)$ obtained with FT (solid curve) and RM for $K=37$ (dashed curve). Case *P*IIa (Re =70.73, Ra=18 000). Instantaneous flows at times t_1 and t_2 are shown in Fig. 14.

does not reduce the computational effort, but could yield insight on optimizing the RM technique. (We note that POD models incorporate high-amplitude modes by construction, but they may not span the space of all possible initial conditions and do not necessarily converge to the correct dynamics [9].)

A number of authors have shown that modes of low amplitude may nevertheless be crucial in the dynamics. Examples abound in which the inclusion of additional modes or the exclusion of a low-amplitude mode substantially worsens agreement [2,3,11,12]. Our experience confirms this, and we report the results of our numerical experiments below.

As described in the previous section, the value of K considered was varied depending on the case under study, limiting K to 41. In simple cases close to the threshold as in *S*I and *P*Ia, K as small as 15 can be chosen. Further from threshold (*S*II and *P*Ib), the value of K used was increased to 41 and 27, respectively, to obtain reasonable solutions. In cases *P*IIa, *P*IIb, and *P*III, for which the behavior of the temporal solution becomes complicated, K was then increased to 37, 40, and 27, respectively. It is intuitive that K must increase with the complexity of the temporal signal, but *S*II case reveals that, even in the stationary case, many modes can be required.

Figures 16(a) and 16(c) show the values of $|A_k|$ in the stationary cases *S*I and *S*II, respectively. Note that two consecutive A_k of the same magnitude form a complex-conjugate pair. Figure 16(a) shows that the A_k's which contribute substantially to the final stable state are concentrated in the first modes, lending support to our approach. The first 15 leading eigenvalues have been considered in the computations [Fig. 7(a)] but, as observed in Fig. 16(b), including

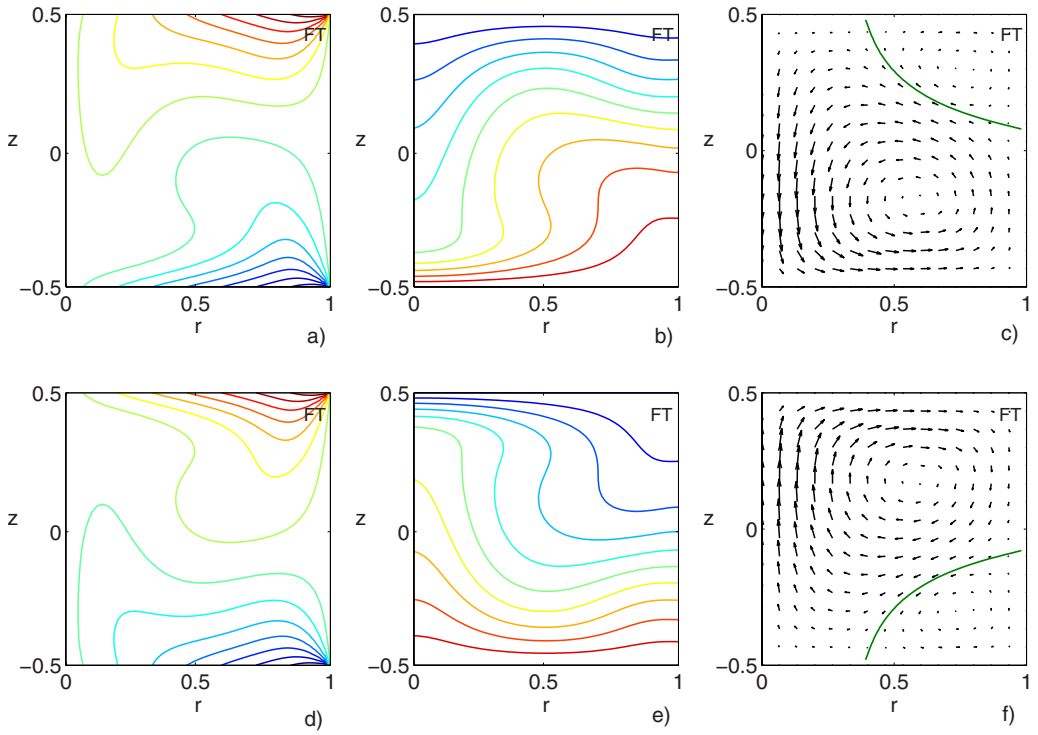

FIG. 14. (Color online) Instantaneous flows for *P*IIa (Re=70.73, Ra=18 000). Upper row: flow at instant $t=t_1$ of Fig. 13. (a) u_ϕ (b) Θ (c) meridional velocity (u_r,u_z). Lower row: flow at $t=t_2$ (d) u_ϕ (e) Θ (f) meridional velocity (u_r,u_z). In Figs. 14(c) and 14(f) the solid green curve represents the streamline separating the rolls.

only the eight eigenvectors with largest $|A_k|$ is sufficient since the resulting solution is almost the same as that constructed from the first 15 eigenvectors. In the case *S*II, the entire set of the first 41 leading eigenvalues must be retained.

We now discuss the requirements on K in the near-sinusoidal periodic cycle case as Ra is increased away from the threshold by comparing cases *P*Ia and *P*Ib. Figure 17 shows the values of $\max_t|A_k(t)|$ for *P*Ia at $(\mathrm{Re},\mathrm{Ra})=(110,18\,000)$ and for *P*Ib at $(\mathrm{Re},\mathrm{Ra})=(110,24\,000)$, respectively. The first two eigenvalues, $k=1$ and 2, are the complex-conjugate pair to which the basic state is unstable in this parameter region. As Fig. 11 has shown, 15 modes give satisfactory results for *P*Ia. Figure 17(b), with $k=[1,2,5]$ shows that the inclusion of mode 5 can saturate the growth of modes 1 and 2, although with large error in amplitude and period.

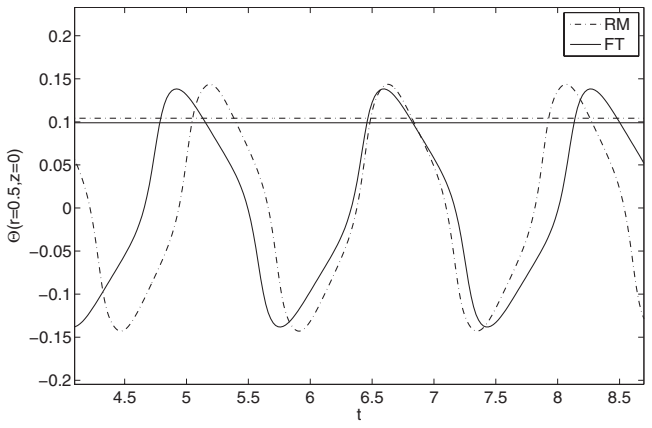

FIG. 15. Time series for $\Theta(0.5,0)$ obtained with FT (solid curve) and RM for $K=27$ (dashed curve). Case *P*III (Re =88.5, Ra=13 000). For both FT and RM, either a steady state or a periodic orbit can be reached, depending on initial conditions.

Case *P*Ib best demonstrates the inadequacy of a criterion based on the amplitude of $\max_t|A_k(t)|$, which we will denote merely by A_k for brevity. Figure 17(c) shows how the values of A_k at large k increase with the distance from threshold, as in the stationary case. Figure 17(d) shows time series obtained by FT and truncations of RM. As mentioned in Sec. V C, the time series obtained by using 27 leading eigenmodes is extremely close to that of FT. Drastically truncating the basis set to retain only the five largest components, $k\in[1,2,5,13,7]$ (listed in order of magnitude of A_k) yields a periodic time series, but whose amplitude exceeds that of FT by almost 60%. Expanding the set to include the five next largest components, $k\in[1,2,5,13,7,3,4,26,27,10]$, yields a limit cycle whose amplitude is too small by 25%. If we exclude the complex pair $k=3$ and 4 to form the set $k\in[1,2,5,13,7,26,27,10]$, we obtain the time series illustrated in Fig. 17(d). The signal saturates at an amplitude close to that of FT, although the period still shows some error. However, excluding the smaller-magnitude complex pair $k=26$ and 27 leads to the time series in Fig. 17(d) which diverges at $t\sim1.3$; these modes seem to be important for stabilizing the flow. This shows the failure of a criterion based on the amplitude of A_k. Similar erratic convergence behavior is reported and analyzed in [2–4,9,11] for POD and for eigenvector models.

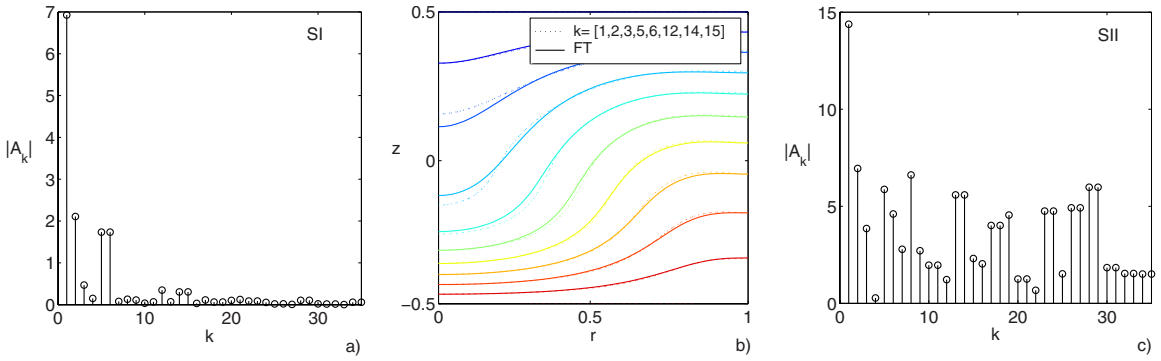

FIG. 16. (Color online) (a) $|A_k|$ values for *S*I (Re=30, Ra=4000); (b) isotherm comparison for *S*I using FT and RM with k values [1–3,5,6,12,14,15]; and (c) $|A_k|$ values for *S*II (Re=60, Ra=18 000);

For a near-heteroclinic cycle as in *P*IIa and *P*IIb, many modes are required. The maximum value of the A_k's over a period are presented in Fig. 18. Inclusion of the entire set of 37 leading eigenvalues (K=37) is required to capture the heteroclinic cycle shown in Fig. 13. Any smaller set of selected eigenmodes is unable to reproduce the time series. For the last case under study, *P*III, no large values of A_k are found at large k [see Fig. 18(b)] but we have found that K =27 is the minimum number of modes necessary to accurately reproduce periodic and asymmetric steady solutions.

VII. CONCLUSIONS

A technique to reduce the number of degrees of freedom to less than 41 has been derived for Rayleigh-Bénard convection in cylindrical geometry with counter-rotating disks. For various Rayleigh and Reynolds numbers, rich and complex dynamics could be reproduced. Even if this success is restricted in our study to a specific case, we hope that this example is relevant to a certain class of configurations, namely bifurcations of flows in confined geometry for moderately stiff problems. We have shown the feasibility of building a RM technique for time integration. For a given set of (Re, Ra) values, time integration starting from many initial conditions can be carried out economically.

Although our study shows that we can reduce the number of degrees of freedom to a small fraction of that of a fully resolved simulation, there is, however, at present no reliable criterion for determining the number of eigenvectors that

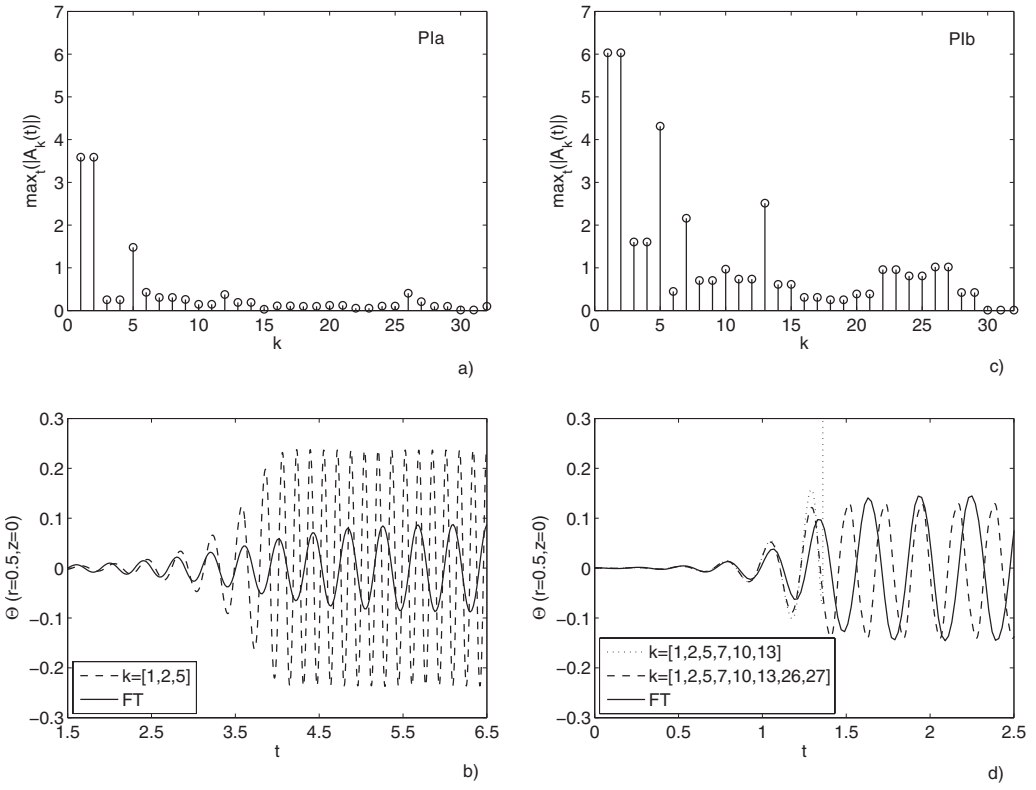

FIG. 17. (a) $\max_t|A_k(t)|$ values for *P*Ia (Re=110, Ra=18 000). (b) Time series comparison using FT (solid curve) and RM (dashed curve) with k values [1,2,5]. (c) $\max_t|A_k(t)|$ values for *P*Ib (Re=110, Ra=24 000). (d) Time series comparison using FT (solid curve) and RM with k values [1,2,5,7,10,13] (dotted curve) and [1,2,5,7,10,13,26,27] (dashed curve). The time series diverges for the smaller k set.

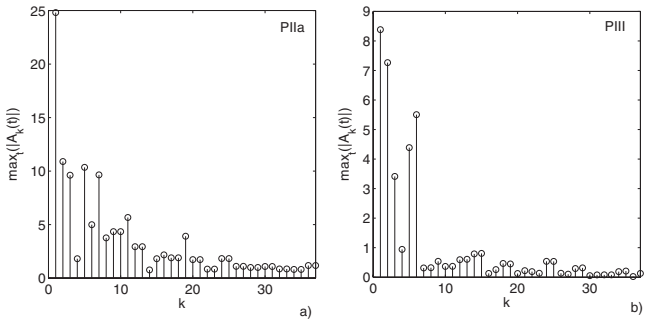

FIG. 18. $\max_t|A_k(t)|$ values for (a) *P*IIa (Re=70.73, Ra =18 000); (b) *P*III (Re=88.5, Ra=13 000).

must be retained. Beyond a minimal K value, we nevertheless observed a slow but monotonic convergence with K. Capturing the interaction between eigenmodes is crucial; as discussed in Sec. VI, these interactions are not easy to follow and improvement of the reduced model still requires additional research.

In order to fully describe and understand bifurcation scenarios, time integration is insufficient. Instead, bifurcation analysis is performed via a combination of Newton's method to follow stable and unstable branches and the Arnoldi method to perform linear stability analysis along the branches and detect bifurcations, which can be quite costly. Our eventual goal is to extend the RM technique to carry out bifurcation analysis, using sophisticated tools for bifurcation analysis, such as MatCont [30] and Auto [31], on the reduced set of ODEs. A crucial obstacle to this plan is that the basic state and K leading direct and adjoint eigenpairs, i.e., steps 1 and 2, must be recomputed for each set of (Re, Ra) values. In order to extend the RM technique to carry out bifurcation analysis, it would be essential to interpolate basis functions from those calculated at a few points of the (Re, Ra) plane. This is a direction of investigation in the near future.

Although the reduced model technique currently requires more computation time than full simulation, it has yet to be optimized. In addition, we have some confidence that extending RM to non-axisymmetric flow is realistic. In a cylindrical geometry, the azimuthal direction can be represented using Fourier series. For an axisymmetric base flow, the eigenmodes associated with each azimuthal wave number can be computed independently; the nonlinear interaction associated with different wave numbers is sparse as well. This extension would then provide a fast three-dimensional time-integration code advantageous for flow control applications that require real-time simulation.

ACKNOWLEDGMENTS

M.C.N. acknowledges support from CCYT (JC de Castilla-La Mancha). The authors have benefited from discussions with O. Le Maître, L. Mathelin, B. Podvin, and J. S. Walker.

APPENDIX

1. Evolution equations for perturbation and direct system

The evolution equations for the perturbation are obtained substituting Eq. (7) into the equations and boundary conditions (1)–(6),

$$\nabla \cdot \tilde{\mathbf{u}} = 0, \tag{A1}$$

$$\partial_t \tilde{\Theta} = \underbrace{-\tilde{\mathbf{u}} \cdot \nabla \Theta^b - \mathbf{u}^b \cdot \nabla \tilde{\Theta} + \nabla^2 \tilde{\Theta}}_{\mathcal{L}_{U^b}} \underbrace{- \tilde{\mathbf{u}} \cdot \nabla \tilde{\Theta}}_{\mathcal{N}}, \tag{A2}$$

$$\partial_t \tilde{\mathbf{u}} = \underbrace{-(\tilde{\mathbf{u}} \cdot \nabla)\mathbf{u}^b - (\mathbf{u}^b \cdot \nabla)\tilde{\mathbf{u}} + \mathrm{Pr}(-\nabla \tilde{p} + \nabla^2 \tilde{\mathbf{u}} + \mathrm{Ra}\tilde{\Theta}\mathbf{e}_z)}_{\mathcal{L}_{U^b}} \underbrace{- (\tilde{\mathbf{u}} \cdot \nabla)\tilde{\mathbf{u}}}_{\mathcal{N}}, \tag{A3}$$

$$\tilde{u}_r = \tilde{u}_\phi = \tilde{u}_z = \tilde{\Theta} = 0 \quad \text{at} \quad z = \pm 1/2, \tag{A4}$$

$$\tilde{u}_r = \tilde{u}_\phi = \partial_r \tilde{u}_z = \partial_r \tilde{\Theta} = 0 \quad \text{at} \quad r = 0, \tag{A5}$$

$$\tilde{u}_r = \tilde{u}_\phi = \tilde{u}_z = \partial_r \tilde{\Theta} = 0 \quad \text{at} \quad r = \Gamma. \tag{A6}$$

By considering $\tilde{U}(r,z,t) = \tilde{U}(r,z)e^{\lambda t}$ in Eqs. (A1)–(A6) and neglecting the nonlinear terms $(\tilde{\mathbf{u}} \cdot \nabla)\tilde{\Theta}$ in Eq. (A2) and $(\tilde{\mathbf{u}} \cdot \nabla)\tilde{\mathbf{u}}$ in Eq. (A3) we obtain an eigenvalue problem in λ. We will denote by (λ_i, ξ_i) the corresponding eigenvalues and eigenvectors of this problem.

2. Adjoint system

The derivation of the adjoint system is described in [32]. The adjoint eigenvalue problem in λ associated with the linear part of Eqs. (A1)–(A6) is

$$\nabla \cdot \hat{\mathbf{u}} = 0, \tag{A7}$$

$$-\lambda \hat{\Theta} = -\mathbf{u}^b \cdot \nabla \hat{\Theta} - \nabla^2 \hat{\Theta} - \mathrm{PrRa}\hat{\mathbf{u}}\mathbf{e}_z, \tag{A8}$$

$$-\lambda \hat{\mathbf{u}} = -(\mathbf{u}^b \cdot \nabla)\hat{\mathbf{u}} - (\nabla \mathbf{u}^b)^t \hat{\mathbf{u}} + \mathrm{Pr}(-\nabla \hat{p} - \nabla^2 \hat{\mathbf{u}}) + \hat{\Theta} \cdot \nabla \Theta^b, \tag{A9}$$

$$\hat{u}_r = \hat{u}_\phi = \hat{u}_z = \hat{\Theta} = 0 \quad \text{at} \quad z = \pm 1/2, \tag{A10}$$

$$\hat{u}_r = \hat{u}_\phi = \partial_r \hat{u}_z = \partial_r \hat{\Theta} \quad \text{at} \quad r = 0, \tag{A11}$$

$$\hat{u}_r = \hat{u}_\phi = \hat{u}_z = \partial_r \hat{\Theta} = 0 \quad \text{at} \quad r = \Gamma. \tag{A12}$$

We will denote by (λ_i, η_i) the corresponding eigenvalues and eigenvectors.

[1] B. R. Noack, K. Afanasiev, M. Morzynski, G. Tadmor, and F. Thiele, J. Fluid Mech. **497**, 335 (2003).
[2] C. W. Rowley, T. Colonius, and R. M. Murray, Physica D **189**, 115 (2004).
[3] C. W. Rowley, Int. J. Bifurcation Chaos Appl. Sci. Eng. **15**, 997 (2005).
[4] B. R. Noack, P. Papas, and P. A. Monkewitz, J. Fluid Mech. **523**, 339 (2005).
[5] M. Bergmann, L. Cordier, and J. P. Brancher, Phys. Fluids **17**, 097101 (2005).
[6] B. Podvin, Phys. Fluids **21**, 015111 (2009).
[7] B. Podvin and P. Le Quéré, Phys. Fluids **13**, 3204 (2001).
[8] H. Gunes, Fluid Dyn. Res. **30**, 1 (2002).
[9] D. Rempfer, Theor. Comput. Fluid Dyn. **14**, 75 (2000).
[10] E. Åkervik, J. Hoepffner, U. Ehrenstein, and D. S. Henningson, J. Fluid Mech. **579**, 305 (2007).
[11] A. Barbagallo, D. Sipp, and P. Schmid, J. Fluid Mech. **641**, 1 (2009).
[12] A. K. Bangia, P. F. Batcho, I. G. Kevrekidis, and G. E. Karniadakis, SIAM J. Sci. Comput. (USA) **18**, 775 (1997).
[13] P. C. Dauby, P. Colinet, and D. Johnson, Phys. Rev. E **61**, 2663 (2000).
[14] J. H. Siggers, J. Fluid Mech. **475**, 357 (2003).
[15] E. Gadoin, P. Le Quéré, and O. Daube, Int. J. Numer. Methods Fluids **37**, 175 (2001).
[16] G. S. Charlson and R. L. Sani, Int. J. Heat Mass Transfer **13**, 1479 (1970).
[17] C. Nore, M. Tartar, O. Daube, and L. S. Tuckerman, J. Fluid Mech. **511**, 45 (2004).
[18] L. Bordja, L. S. Tuckerman, L. Martin Witkowski, M. C. Navarro, D. Barkley, and R. Bessaih, Phys. Rev. E **81**, 036322 (2010).
[19] H. Herrero and A. M. Mancho, Int. J. Numer. Methods Fluids **39**, 391 (2002).
[20] P. Manneville, *Dissipative Structures and Weak Turbulence* (Academic, New York, 1990).
[21] C. Bernardi and Y. Maday, *Approximations Spectrales de Problèmes aux Limites Elliptiques* (Springer-Verlag, Berlin, 1991).
[22] C. Canuto, M. Y. Hussain, A. Quarteroni, and T. A. Zang, *Spectral Methods in Fluid Dynamics* (Springer, Berlin, 1988).
[23] J. M. Lopez, F. Marques, and J. Sanchez, J. Fluid Mech. **439**, 109 (2001).
[24] M. C. Navarro, H. Herrero, A. M. Mancho, and A. Wathen, Commun. Comput. Phys. **3**, 308 (2008).
[25] R. B. Lehoucq, D. C. Sorensen, and C. Yang, *ARPACK Users' Guide: Solution of Large Scale Eigenvalue Problems with Implicitly Restarted Arnoldi Methods* (SIAM, Philadelphia, 1998).
[26] M. C. Navarro, A. M. Mancho, and H. Herrero, Chaos **17**, 023105 (2007).
[27] O. Daube, in *Vortex Dynamics and Vortex Methods*, Lectures in Applied Mathematics, edited by C. R. Anderson and C. Greengard (American Mathematical Society, Providence, RI, 1991), Vol. 28, pp. 131–152.
[28] J. N. Sorensen and T. Phuoc Loc, Int. J. Numer. Methods Fluids **9**, 1517 (1989).
[29] L. Martin Witkowski, P. Marty, and J. S. Walker, J. Fluid Mech. **436**, 131 (2001).
[30] A. Dhooge, W. Govaerts, and Yu. A. Kuznetsov, ACM Trans. Math. Softw. **29**, 141 (2003).
[31] E. J. Doedel, R. C. Paffenroth, A. R. Champneys, T. F. Fairgrieve, Yu. A. Kuznetsov, B. Sandstede, and X. Wang, *AUTO 2000: Continuation and bifurcation software for ordinary differential equations (with HomCont), Technical Report* (Caltech, Pasadena, CA, 2001).
[32] O. Bouizi and C. Delcarte, Int. J. Numer. Methods Fluids **50**, 947 (2006).